Monthly Notices
of the
ROYAL ASTRONOMICAL SOCIETY

Mon. Not. R. Astron. Soc. **426,** 2847–2858 (2012) doi:10.1111/j.1365-2966.2012.21515.x

Optical polarization of quasars and the Balmer edge feature revealed by ultraviolet and polarized visible to near-infrared emissions

Renyu Hu[1] and Shuang-Nan Zhang[2,3]★

[1]*Department of Earth, Atmospheric and Planetary Sciences, Massachusetts Institute of Technology, Cambridge, MA 02139, USA*
[2]*Key Laboratory of Particle Astrophysics, Institute of High Energy Physics, Chinese Academy of Sciences, Beijing 100049, China*
[3]*Space Science Division, National Astronomical Observatories of China, Chinese Academy of Sciences, Beijing 100012, China*

Accepted 2012 June 12. Received 2012 June 5; in original form 2012 April 24

ABSTRACT

Polarized emission from a quasar is produced by wavelength-independent electron scattering that surrounds its accretion disc. Thus, contamination from the host galaxy is avoided and the intrinsic emission spectrum of its accretion disc is revealed. Ultraviolet (UV) emission from a quasar is normally free of contamination from its host galaxy. Therefore, the polarization fraction of the quasar's disc emission can be determined by comparing the total UV emission with the polarized visible to near-infrared (NIR) emission. The resulting continuum spectrum from UV to infrared can reveal the theoretically expected Balmer edge absorption feature. We fit the polarized spectra in the visible and NIR bands, together with the total UV spectra of two type 1 quasars (3C 95 and 4C 09.72), to an extended geometrically thin and optically thick accretion disc model. In addition to the standard model, we include the Balmer edge absorption that results from corotational neutral gas on a narrow annulus of the accretion disc. We find that the extended thin accretion disc model provides an adequate description of the continuum spectra of the two quasars from UV to NIR wavelengths. A Monte Carlo–Markov chain fitting to the continuum spectra is able to constrain well the true polarization fraction of the disc emission, which allows the Balmer edge feature to be completely revealed from polarized visible to UV continua. The Balmer edge feature is prominent in the spectra of both quasars, and it is significantly broadened because of the orbital motion of the gas in the accretion disc. Therefore, the broadening of the Balmer edge feature is related to the quasar's inclination. In this paper, we prove the concept of determining a quasar's inclination from the Balmer edge feature in its continuum spectra.

Key words: methods: data analysis – techniques: polarimetric – techniques: spectroscopic – galaxies: active – quasars: general.

1 INTRODUCTION

Quasars are the most luminous objects in the Universe. The release of gravitational energy, as material is accreted on to the supermassive black hole (SMBH), heats the accretion disc and generates multicolour thermal emission from ultraviolet (UV) to infrared (IR) wavelengths (e.g. Novikov & Thorne 1973; Shakura & Sunyaev 1973; Lynden-Bell & Pringle 1974; Loar & Netzer 1989; Loar, Netzer & Piran 1990; Hubeny et al. 2000). However, the total emission of a quasar at visible and near-IR (NIR) wavelengths is mixed by emissions from both its accretion disc, which surrounds its central SMBH, and its host galaxy, which complicates observations of the intrinsic emission of the quasar's accretion disc. For example, the optically thick and geometrically thin standard disc model predicts that the emission spectrum in the optical to NIR should follow $F_\nu \propto \nu^\alpha$, where F_ν is the flux per frequency, ν is the frequency and $\alpha = 1/3$ (e.g. Shakura & Sunyaev 1973; Lynden-Bell & Pringle 1974). However, many quasar spectra in the optical to NIR have $\alpha < -0.2$ (Neugebauer et al. 1987; Cristiani & Vio 1990; Francis et al. 1991; Zheng et al. 1997), consistent with significant contaminations from the host galaxy, which are increasingly important at longer wavelengths.

The polarized spectra of quasars at visible and NIR wavelengths might reveal the emissions of their accretion discs, because polarization is expected to come from the electron scattering inside the broad line region (BLR) and the electron scattering is wavelength-independent. Kishimoto et al. (2008) have reported on the polarized

★E-mail: zhangsn@ihep.ac.cn

spectra of six quasars in the rest wavelength ranging from 0.2 to 2 μm. These quasars have ∼1 per cent of polarization in the optical bands, less than 1 per cent of polarization in the NIR continuum and little polarization in their emission lines. Indeed, Kishimoto et al. (2008) have found that the polarized NIR spectra manifest $\alpha = 1/3$, as expected from the standard disc model. We emphasize two important facts regarding the quasar polarization at visible and NIR wavelengths. First, the alignment of the optical polarization with the radio structure of many quasars suggests that the emission is polarized not in the disc atmosphere but in an equatorial scattering region surrounding the disc (e.g. Stockman, Angel & Miley 1979; Smith et al. 2005). Indeed, the intrinsic polarization produced in the disc atmosphere is likely to be damped by Faraday rotation (e.g. Agol & Blaes 1996). Secondly, the observed polarization percentage in the optical to NIR bands might not be the polarization percentage of the intrinsic disc emission, or the polarization percentage of the equatorial scattering region, because of possible contamination from the quasar's host galaxy.

The standard thin disc model predicts a bump shape from UV to visible wavelengths, which is produced by the emission from the inner disc region and is determined by the combination of the mass of the central SMBH and the boundary radius of the inner disc. The UV continuum is relatively free of contamination from the host galaxy, and thus it should reflect the emergent spectra of the accretion disc and allow us to probe the inner part of the accretion disc. Two quasars from the sample of Kishimoto et al. (2008), 3C 95 and 4C 09.72, have been observed with the *Hubble Space Telescope* (*HST*) and their UV spectra have been published (Bahcall et al. 1993; Marziani et al. 1996; Evans & Koratkar 2004). Therefore, combining the UV continuum and the polarized spectra in visible and NIR wavelengths will provide a powerful spectral diagnosis of the nature of the SMBHs and accretion discs of the two quasars. It has also been reported that the quasar continuum spectra in wavelengths shorter than 120 nm can be described by a simple power law with the index $\alpha_{\rm EUV} = -1.76 \pm 0.12$. This suggests that the extreme UV (EUV) continuum is probably a result of the intergalactic medium photoionized by the integrated radiation from quasars (Telfer et al. 2002). Therefore, the EUV continuum might not reflect the intrinsic emission of a quasar's accretion disc.

The continuum spectra of quasars from UV to NIR wavelengths can be used to constrain the properties of their central SMBHs, in particular their BH spin, in a similar way to the method used for stellar mass BHs in X-ray binaries; the BH mass and disc inclination angle (i) are very well known for some X-ray binaries (Zhang, Cui & Chen 1997; Shafee et al. 2006). Czerny et al. (2012) have used the standard thin accretion disc model to fit several broad-band photometric points of the quasar SDSS J094533.99+100950.1. Assuming a BH mass, this procedure puts constraints on its spin. However, the broad-band photometric fluxes might be contaminated by broad spectral lines, which might affect the estimates of the BH spin. Davis & Loar (2011) have also used the thin accretion disc model to fit the shape of the optical continuum of a set of 80 Palomar–Green (PG) quasars, and they have obtained their radiative efficiency and derived their BH spin. However, in both methods, the BH mass and the inclination angle of the accretion disc had to be assumed a priori. Various methods can be used to estimate the BH mass in a quasar, but normally within a factor of 2–3, as discussed in Section 4.1.

The inclination of the accretion disc for an individual quasar is normally not well constrained. According to the unified model of active galactic nuclei (AGNs), the emission from a quasar's accretion disc is not blocked by its dusty torus, which implies a disc inclination of less than ∼60° (e.g. Antonucci 1993). An advanced torus model and a spectroscopy of quasars in the mid-infrared wavelengths might provide more insights on the interaction of the disc emission and the torus and better constrain the disc inclination (e.g. Alonso-Herrero et al. 2011). Another method to determine the disc inclination is to describe not only the spectra but also the morphology of active galaxies self-consistently (Kacprzak et al. 2011). For radio-loud objects, the inference of the radio core luminosity might constrain the view angle of the radio source (i.e. the inclination of the accretion disc; e.g. Wills & Brotherton 1995). However, the disc inclination has not been estimated from the disc emission directly. In principle, the luminosity of the accretion disc scales as $\cos(i)$, so the inclination might be constrained by photometry if the BH mass and accretion rate can be independently estimated (e.g. Czerny et al. 2012). So far, this method has large uncertainty, mainly because of the large uncertainty of the BH mass.

The comparison between a quasar's UV emission and its polarized visible emission can be complicated by the possible Balmer edge absorption. It has been reported that the polarized fluxes of the two quasars manifest a discontinuity in the slope at wavelengths shorter than ∼400 nm (Kishimoto et al. 2004). The feature is mostly interpreted as the buried Balmer edge of the intrinsic spectra of the quasar UV/optical continuum, or the big blue bump (BBB) emission. The edge absorption feature is a result of the bound-free opacities in the disc's atmosphere, and indeed it indicates the thermal and optically thick nature of the continuum. However, the origin of the Balmer edge absorption is still unknown. An order-of-magnitude estimate of the broadening of the Balmer edge indicates that the broadening is consistent with the orbital motion of the corresponding disc annuli responsible for emission around 400 nm (Kishimoto et al. 2004).

In this paper, we use the extended standard thin accretion disc model to fit the polarized spectra in the visible and NIR bands and the total spectra in the UV band of 3C 95 and 4C 09.72, after removing prominent emission and absorption features; the extension includes the Balmer edge absorption of an optically thin layer of neutral gas corotating with the accretion disc. We use the Monte Carlo–Markov chain (MCMC) method to fully explore the multi-dimensional parameter space of the BH mass, spin, accretion rate, disc inclination and polarization. The wide spectral coverage of the total UV emission and the polarized spectra in the visible and NIR bands provides a complete description of the accretion disc emission, which allows us to determine of physical properties of the BH and the accretion disc. In particular, the true polarization fraction of the disc emission can be well constrained from the spectral fitting, which leads to a continuum spectrum from UV to NIR. The spectral fitting also constrains the broadening of the Balmer edge, which is controlled by the disc inclination.

2 STANDARD ACCRETION DISC MODEL WITH BALMER EDGE

We intend to describe the polarized spectra in the visible and NIR wavelengths as well as the total spectra in UV wavelengths using the standard thin disc model (Shakura & Sunyaev 1973; Lynden-Bell & Pringle 1974). As an extension to the standard model, we include the Balmer edge absorption of the neutral gas that is assumed to be corotating with the accretion disc. Because of the extensive computation burden, we do not intend to model in detail the atmosphere of the accretion discs of quasars (e.g. Loar & Netzer 1989; Loar et al. 1990; Hubeny et al. 2000). Our main goal is to determine the BH parameters from the continuum of quasars.

According to the standard thin disc model, the temperature of the accretion disc follows (Krolik 1998; Hubeny et al. 2000)

$$T(x) = \left[\frac{3GM_{\rm BH}\dot{M}}{8\pi\sigma r^3}R_R(r)\right]^{1/4} = 5.9\times10^7\,\eta^{-1/4}\left(\frac{L}{L_{\rm EDD}}\right)^{1/4} \times\left(\frac{M_{\rm BH}}{\rm M_\odot}\right)^{-1/4} x^{-3/4}R_{\rm R}(x)^{1/4}\,({\rm K}), \quad (1)$$

where T is the temperature, G is the gravitational constant, $M_{\rm BH}$ is the BH mass, $\dot{M}$ is the accretion rate, σ is the Stefan–Boltzmann constant, r is the radius, x is the radius in units of gravitational radius $r_{\rm g} = GM_{\rm BH}/c^2$, η is the radiative efficiency as a function of BH spin a/M, $L/L_{\rm EDD}$ is the accretion rate in units of the Eddington accretion rate and $R_{\rm R}$ is the correction term of the general relativistic (GR) effects, analytically expressed as a function of a/M (see Krolik 1998). The analytical expressions of η and $R_{\rm R}$ are given in Appendix A.

We assume that the Balmer edge absorption comes from a relatively narrow disc annuli for an effective temperature from 8000 to 20 000 K, based on the consideration of the $n = 2$ population of hydrogen. The ionization of hydrogen depends on the number density in the photosphere, which in turn depends on the torque of the disc, an observational unknown. With a sensible range of the torque value, a realistic disc vertical structure model (Loar & Netzer 1989) and the local thermal equilibrium of a pure hydrogen plasma, we find that the $n = 2$ population is concentrated in a relatively narrow range, with a temperature of 8000–20 000 K. A large electron density from the ionization of metals, and a range of other parameters, might affect the temperature range of the $n = 2$ population; we have performed a sensitivity study by allowing the Balmer edge absorption to occur in annuli of $T = 8000$–15 000 to 25 000 K. The frequency-dependent form of the Balmer edge feature is

$$\tau(\nu) = 0, \quad (\nu < \nu_c)$$
$$\tau(\nu) = \frac{\tau_0}{\mu}\left(\frac{\nu}{\nu_c}\right)^{-2.67}, \quad (\nu > \nu_c). \quad (2)$$

Here, τ_0 is the characteristic optical depth as a result of the common photoelectric absorption, ν_c is the threshold frequency corresponding to ∼364.6 nm and $\mu \equiv \cos(i)$, where i is the inclination angle of the accretion disc. For simplicity, we assume that τ_0 is a constant in the Balmer absorption annuli, and zero elsewhere. Given L, $M_{\rm BH}$ and a/M, the range of radii of Balmer absorption annuli x_0 can be found by allowing $T = 8000$–20 000 K in equation (1).

The inclination of the accretion disc has three effects: local limb darkening, projection of the disc on the sky plane and the relativistic Doppler effect as a result of the orbital motion. Omitting the GR effect of photon propagation, the asymmetric broadening factor as a result of the orbital motion is derived as

$$S(\nu,\nu_0) = \frac{1}{\pi}\frac{\nu^3}{\nu_0^4\gamma}\frac{1}{\sqrt{\beta_1^2-[1-(\nu/\nu_0\gamma)^2]}}, \quad \nu_0\gamma(1-\beta_1) < \nu < \nu_0\gamma(1+\beta_1), \quad (3)$$

where ν is the observed frequency, ν_0 is the emission frequency in the rest frame of the rotating gas, $\gamma_0 \equiv 1/\sqrt{1-\beta_0^2}$, β_1 is the relativistic factor corrected for the inclination as $\beta_1 = \beta_0\sin(i)$, $\beta_0 \equiv v_0/c$ and v_0 is the local Keplerian velocity of the disc where the Balmer absorption takes place. Here, we can see that the broadening of the Balmer edge feature sensitively depends on the disc's inclination. In the Newtonian regime, $\beta = x^{-1/2}$. In the Kerr space–time, β is an analytical function of x and a/M (see Krolik 1998, for a detailed formulation). We verify that when x is large, the functional form of β in the Kerr space–time approaches that of the Newtonian regime.

The emerging spectrum from an optically thick disc with an optically thin layer of absorbing neutral gas is then described by

$$\nu L_\nu = \nu\int_{x_{\rm in}}^{x_{\rm out}} f(x,\nu)2\pi x\,{\rm d}x \times \frac{3}{4}\left(\mu+\frac{2}{3}\right)\mu, \quad (4)$$

where the local limb darkening and the projection of the disc plane are considered as they are in Krolik (1998). The inner edge of the accretion disc ($x_{\rm in}$) is assumed to be located at the innermost circular orbit of the spinning BH, as a function of a/M. The analytical expression of $x_{\rm in}$ is given in Appendix (A). In our calculation, we choose $x_{\rm out} = 1000$, which is large enough to compute the NIR spectra up to 2 μm. Thus, $f(x, \nu)$, which is the emission flux from an annuli between x and $x + {\rm d}x$, can be computed from the following integration

$$f(x,\nu) = \int_{\nu/\gamma(1+\beta_1)}^{\nu/\gamma(1-\beta_1)} B\,[T(x),\nu_0]\exp\,[-\tau(\nu_0)]\,S(\nu,\nu_0)\,{\rm d}\nu_0, \quad (5)$$

where $B(T, \nu)$ is the Planck function. The observed polarized spectrum in the optical and NIR wavelengths ($\nu F_{\nu,{\rm OIR}}$) and the UV continuum ($\nu F_{\nu,{\rm UV}}$) are then

$$\nu F_{\nu,{\rm OIR}} = P\frac{\nu L_\nu}{D^2}, \qquad \nu F_{\nu,{\rm UV}} = \frac{\nu L_\nu}{D^2}, \quad (6)$$

where P is the polarization fraction and D is the luminosity distance. The luminosity distance to a source is calculated from the redshift z with the standard flat cosmology model of ($\Omega_{\rm M} = 0.3$, $\Omega_\Lambda = 0.7$) and the Hubble constant $H_0 = 72\ {\rm km\ s^{-1}\ Mpc^{-1}}$.

In summary, our model computes the continuum spectrum from UV to NIR of the thin accretion disc with the effect of corotating optically thin Blamer edge absorption. The model involves six independent parameters: the BH mass $M_{\rm BH}$, the BH spin a/M, the accretion rate L, polarization P, inclination i and the optical depth of the Balmer absorption τ_0. In this paper, we use the kinetics of the BLR and the velocity dispersion to determine the BH mass, which decreases the number of free parameters to five. We further define the 'effective' accretion rate as $L' \equiv L \times (3/4)[\mu + (2/3)]\mu$, according to equation (4), in order to remove the correlation between the accretion rate and the inclination. Finally, a/M, L', P, i and τ_0 are our five independent fitting parameters. We emphasize that the formulation here is a simplified treatment of the emission continuum of the accretion discs of quasars. This formulation is computationally efficient, which allows an extensive exploration of the parameter space using the MCMC method.

3 DATA SELECTION

We obtain the total-light and polarized spectra of Q0144–3938, 3C 95, CTS A09.36, 4C 09.72, PKS 2310–322 and Ton 202 in the visible and NIR wavelengths from Kishimoto et al. (2008). The optical spectropolarimetry was taken with the instrument FORS1 mounted on the Very Large Telescope (VLT) UT2 and the Low Resolution Imaging Spectrograph (LRIS) on the Keck-I telescope (Kishimoto et al. 2004, 2008). Both 3C 95 and 4C 09.72 were observed with the VLT in 2002 September, Q0144–3938, CTS A09.36 and PKS 2310-322 were observed with the VLT in 2005 September and Ton 202 was observed with the LRIS on the Keck-I telescope on 2003 May 4.

The NIR broad-band imaging polarimetry of the six quasars was obtained with the UFTI (with the polarimetry module IRPOL2) and

ISAAC instruments, which are mounted on the United Kingdom Infrared Telescope (UKIRT) and the VLT UT1, respectively. Ton 202 was observed with the UKIRT on 2001 January 16 (Kishimoto, Antonucci & Blaes 2005). Both 3C 95 and 4C 09.72 were observed with the UKIRT in the autumn of 2006 and Q0144–3938, CTS A09.36 and PKS 2310–322 were observed with the VLT on 2007 August 21.

Among this sample of six quasars, 3C 95 and 4C 09.72 have reduced spectra in the near-UV wavelengths available for scientific interpretations. The total-light spectra of 3C 95 and 4C 09.72 in the UV wavelength were taken by the *HST* Faint Object Spectrograph (FOS) and they are available from the archive of the *HST* High-Level Science Products (Evans & Koratkar 2004). The spectrum of 3C 95 was taken on 1991 December 21, with a total exposure time of 4454 s. The spectrum of 4C 09.72 was taken on 1992 October 12, with a total exposure time of 4751 s, and on 1993 July 7, with an exposure time of 480 s. The UV and optical spectra are recalibrated uniformly with all other *HST* pre-COSTAR (Corrective Optics Space Telescope Axial Replacement) FOS spectrophotometric data for AGNs and quasars, using the up-to-date algorithms and calibration data (Evans & Koratkar 2004). Where possible, multiple observations are combined to produce a single spectrum for each object, with the highest possible signal-to-noise ratio and covering the widest wavelength range. In this paper, we retrieve the recalibrated spectra of 3C 95 and 4C 09.72 in 1140–3300 Å.

The retrieved UV spectra have many prominent emission and absorption lines, and they have a spectral resolution of ∼1 Å. The UV spectra have been processed in the following steps before being taken into the spectral fittings. First, we remove the absorption lines in the UV spectra. For 3C 95, we use the complete sample of absorption lines provided by Bahcall et al. (1993), which contains the central wavelength in the observation frame and the FWHM of each absorption line. We assume a Gaussian profile for each absorption line with three parameters: central wavelength, FWHM and strength. We take the central wavelength and the FWHM from Bahcall et al. (1993), and we fit the UV spectrum to determine the strength. In Table 1, we list the central wavelengths, FWHMs and strengths of all absorption lines. For 4C 09.72, because no list of absorption lines is available from the literature, we do not perform the removal of absorption lines; because the absorption lines are all very narrow with a FWHM less than 3 Å, they are unlikely to affect the fitting to the continuum.

Table 1. Absorption lines removed from the UV spectra of 3C 95. The wavelength is in the observation frame.

λ (nm)	FWHM (nm)	$\lambda F_\lambda \times 10^{11}$ (erg s^{-1} cm^{-2})	Line
1649.02	1.51	0.30	Lyman α
1742.76	1.86	0.18	Lyman α
1749.42	1.65	0.32	Lyman α
1890.00	2.08	0.35	Si IV
1909.82	1.88	0.56	Lyman α
1959.37	1.59	0.58	Lyman α
2025.72	1.94	0.25	Zn II (Mg II)
2099.70	1.84	0.53	C IV
2103.38	1.80	0.43	C IV
2314.49	4.64	0.14	
2382.53	2.04	0.29	Fe II
2586.82	2.04	0.18	Fe II
2600.20	2.13	0.31	Fe II
2755.34	2.04	0.17	
2796.25	2.23	0.35	Mg II
2803.27	2.55	0.25	Mg II
2852.95	2.04	0.19	Mg I

Table 2. Emission lines removed from the UV spectra of 3C 95 and 4C 09.72. The wavelength is in the observation frame.

Object	λ (nm)	FWHM (nm)	$\lambda F_\lambda \times 10^{11}$ (erg s^{-1} cm^{-2})	Line
3C 95	1670.9	25	0.30	Lyβ, O VI
3C 95	1964.9	70	0.80	Lyα
3C 95	1964.9	30	0.50	Lyα
3C 95	2004.5	60	0.30	N V
3C 95	2257.4	50	0.10	Si IV
3C 95	2504.4	90	0.50	C IV
3C 95	2504.4	35	0.30	C IV
3C 95	3084.9	80	0.20	C III]
4C 09.72	2001.9	40	0.15	Si IV
4C 09.72	2220.9	80	0.50	C IV
4C 09.72	2220.9	20	0.75	C IV
4C 09.72	2735.7	40	0.20	C III]

Secondly, we remove the emission lines in the UV spectra. The extraction of emission lines, especially the prominent broad lines, is complicated. Marziani et al. (1996) have discussed the emission-line profiles of 3C 95 and 4C 09.72 in detail. However, in this paper, we only focus on the continuum. Hence, we try to remove the emission lines in a simple way. We use the line identifications and central wavelengths given by the *HST* High-Level Science Products and we remove each emission line by several trial Gaussian profiles. Note that there is no spectral fitting performed here. We test each of the emission lines with several combinations of FWHM and line strength, assuming the Gaussian profiles, and we determine the best line removal by manual inspection. The Gaussian profiles retracted from the UV spectra are tabulated in Table 2. We do not attempt to remove the iron emission lines. For both 3C 95 and 4C 09.72, the Fe II and Fe III pseudo-continua are much weaker than the C IV emission (Marziani et al. 1996). Also, we only use the UV continua for rest-frame wavelengths shorter than ∼200 nm; in this wavelength range, the effect of iron lines on our spectral fitting is minor (e.g. Vestergaard & Wilkes 2001). Finally, for 3C 95 and 4C 09.72, we dismiss the spectrum with a wavelength shorter than 1300 Å in the rest frame, because of the prominent Galactic Lyman α emission and large statistical errors (e.g. Evans & Koratkar 2004), the non-thermal component resulting from Compton scattering in the accretion disc atmosphere (e.g. Hubeny et al. 2001) and possible intergalactic contamination (Telfer et al. 2002). The UV continuum spectra after the absorption and emission-line removal are shown in Fig. 1.

Finally, we transform the spectra into the rest frame by multiplying the flux F_λ by $(1 + z)$ and we present the flux in terms of λF_λ (see the blue curves in Fig. 1). For the purpose of fitting, we also bin the UV spectra with a linear wavelength spacing of 1 nm, as shown in Fig. 1. The uncertainties of the flux are combined by the standard error propagation method.

4 DATA ANALYSIS

4.1 Black hole mass determination

The most direct measurements of BH masses come from the kinematics of the BLRs of AGNs (i.e. the emission-line width δV and

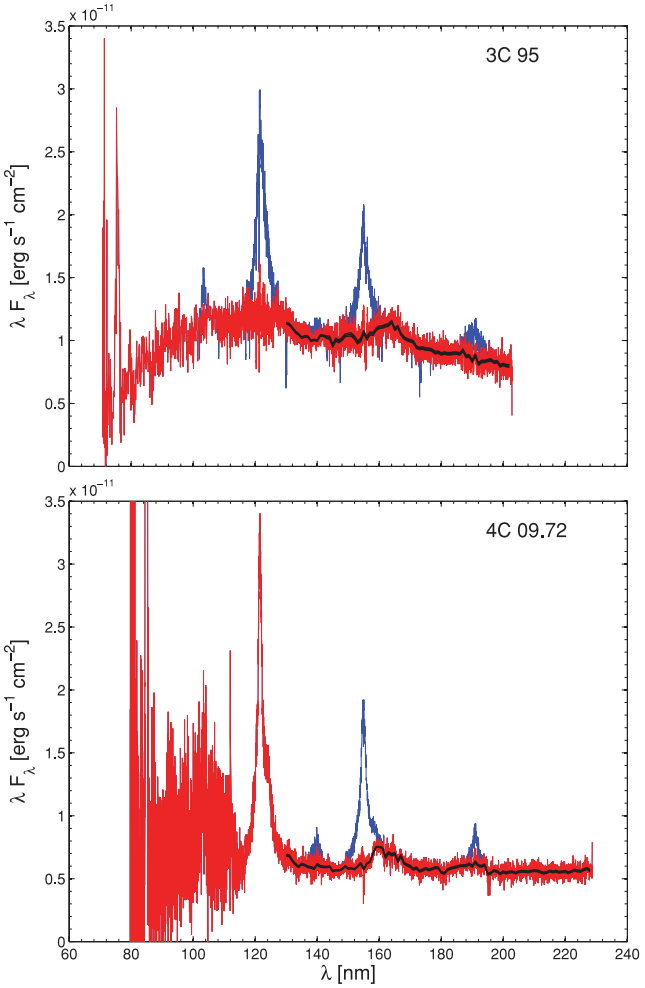

Figure 1. Pre-fitting processes of the UV spectra of 3C 95 and 4C 09.72. The blue curves show the original spectra retrieved from the archive of the *HST* High-Level Science Products with wavelengths in the rest frame. The red curves show the spectra after the emission and absorption lines have been removed. The black curves show the spectra with a linear wavelength spacing of 1 nm.

the size of the BLR given by reverberation mapping; Blandford & Mckee 1982; Peterson 1993), assuming that the line-emitting gas in the BLR is varialized. The virial mass can then be expressed as

$$M_{\rm BH-RM} = \frac{f R \delta V^2}{G}, \tag{7}$$

where f is a factor depending on the structure, kinematics and orientation of the BLR (Peterson et al. 2004). On average, the factor f can be taken as $\langle f \rangle = 5.5$ if the linewidth is taken as the line dispersion $\sigma_{\rm line}$. For a distant AGN, the reverberation measurement is not possible. Then, the BLR size comes from the radius–luminosity (R–L) relationship (i.e. the relationship between the radius of the BLR and the optical luminosity), calibrated at low redshift (Kaspi et al. 2005). The removal of the host galaxy's starlight contribution improves the relationship significantly, and the relationship manifests as $r \propto L^{1/2}$ (Bentz et al. 2006).

The BH mass determined in this way has been found to be tightly correlated with the velocity dispersion of the bulge or spheroid σ_* (the so-called $M_{\rm BH}$–σ_* relation; Ferrarese & Merritt 2000; Tremaine et al. 2002). In this paper, the $M_{\rm BH}$–σ_* relation we have used is determined from the reverberation-mapped virial BH mass, which is provided by Onken et al. (2004). In general, the FWHM of the [O III] λ5007 emission line can be used as a proxy for σ_* (Nelson & Whittle 1996; Nelson 2000).

Although we only perform the spectral fitting to the continuums of 3C 95 and 4C 09.72 in the following, we determine the BH masses for all six quasars in the sample from the BLR kinematics and we compare them with the $M_{\rm BH}$–σ_* relation. In this way, we can verify the reliability of the BH mass determination. We obtain the broad Hβ linewidth by interpolating a linear continuum between continuum windows on either side of the line, and we calculate the line's mean squared dispersion, defined as the second moment of the line profile (Peterson et al. 2004). In practice, the narrow-line residuals significantly influence the determination of the broad-line width. Therefore, we remove the narrow-line component carefully using the adjacent [O III] λ5007 line as a template. The obtained linewidths and BH masses are tabulated in Table 3. The BH masses determined by such a method have typical errors of a factor of 2 (i.e. 0.3 dex; Peterson et al. 2004).

Using the line dispersion of [O III] λ5007 as the probe of the velocity dispersion of the bulge of an AGN's host galaxy, we can plot the obtained BH masses with respect to the established $M_{\rm BH}$–σ_* relation (Tremaine et al. 2002), as in Fig. 2. Using the Nuker estimate, we find that the reduced χ^2 is 1.2, if the errors for $M_{\rm BH-RM}$ and σ_* are taken as 0.3 dex (Peterson et al. 2004) and 0.07 dex (Tremaine et al. 2002), respectively. $M_{\rm BH-RM}$ measures the virial mass of the BH and σ_* indicates the dispersion mass of the BH. The fact that these independent measurements are consistent, as shown in Fig. 2, allows us to conclude that the BH mass estimates from both methods are reliable for these sources. To further improve the accuracy of these BH mass estimates, we combine the BH mass estimates from both methods; the error for the combined BH masses is 0.21 dex. In Table 1, we list the observation data used and the BH masses determined from the reverberation mapping (denoted as $M_{\rm BH-RM}$), the velocity dispersion (denoted as $M_{\rm BH-\sigma}$) and the combined kinematic measurements $\log M_{\rm BH-KM} = 0.5 \times (\log M_{\rm BH-RM} + \log M_{\rm BH-\sigma})$.

4.2 Spectral fitting

We fit the observed continuum spectra of the two quasars (3C 95 and 4C 09.72) to our extended standard thin disc model presented above, with the polarized spectra in the visible and NIR wavelengths, and the total spectra in the UV wavelengths. The polarized spectra are bridged with the total-light spectra by the polarization fraction of the observed accretion disc emission. The five fitting parameters are the BH spin a/M, the accretion rate L', the polarization fraction P, inclination i and the Balmer edge optical depth τ_0. In the fitting, we use the BH mass estimate $M_{\rm BH-KM}$ from Table 3.

We use the MCMC method for the spectral fitting to explore the whole parameter space. Because of the multiparameter nature of the problem, the MCMC method not only provides the possibility of fast computation, but it also gives the posterior probability distribution of all parameters. We use the adaptive Metropolis–Hastings algorithms implemented by Haario et al. (2006).

The convergence of the Markov chain is examined as follows. We start from two randomly selected parameter sets and we generate two Markov chains. The second halves of both chains are mixed together and the so-called potential scale reduction (R) is computed for each estimated parameter (Gelman & Rubin 1992); R declines to unity as the length of Markov chain goes to infinity. In this paper, we require $R < 1.005$ for all estimated parameters as the criterium for the convergence of the Markov chain. We find that this requirement

Table 3. Quasar BH mass estimates.

Quasar name	Hβ width (km s^{-1})	BLR size[a] (light days)	$M_{\rm BH-RM}$ [b] (10^8 M$_\odot$)	σ_* [c] (km s^{-1})	$M_{\rm BH-\sigma}$ [d] (10^8 M$_\odot$)	$M_{\rm BH-KM}$ [e] (10^8 M$_\odot$)	z
Q0144–3938	2570	55.8	3.94	362	14.7	7.6	0.244
3C 95	2846	171.5	14.9	394	20.6	17.5	0.616
CTS A09.36	3124	54.8	5.72	218	1.9	3.3	0.310
4C 09.72	2855	179.8	15.7	359	14.2	14.9	0.433
PKS 2810–322	3048	70.4	7.00	197	1.3	3.0	0.337
Ton 202	3306	77.4	9.05	380	17.8	12.7	0.366

[a]The r–L relationship of Kaspi et al. (2005) is applied.
[b]Estimated from the Hβ width and BLR size, with a 1σ error of 0.3 dec. The factor f is taken as $f = 5.5$.
[c]The velocity dispersion is taken as the line dispersion of [O III] λ5007.
[d]Estimated from σ_*, with a 1σ error of 0.3 dec.
[e]Geometrical average between $M_{\rm BH-RM}$ and $M_{\rm BH-\sigma}$, that is, $\log M_{\rm BH-KM} = 0.5 \times (\log M_{\rm BH-RM} + \log M_{\rm BH-\sigma})$, with a 1$\sigma$ error of 0.21 dec.

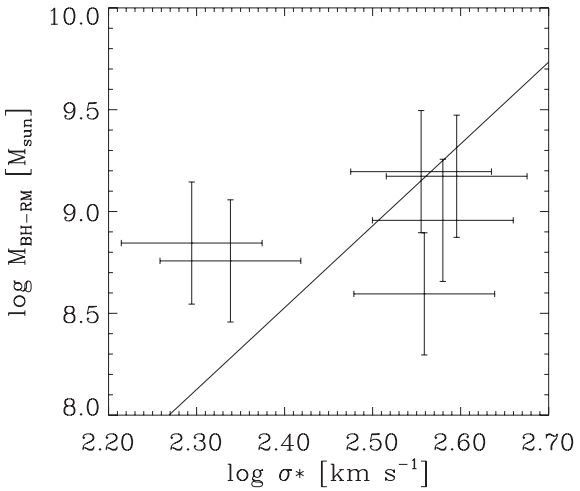

Figure 2. Virial BH masses $M_{\rm BH}$ and velocity dispersion σ_* on $M_{\rm BH}$–σ_* relations. The solid line shows the $M_{\rm BH}$–σ_* relation by Tremaine et al. (2002). The uncertainty of $M_{\rm BH}$ is within a factor of 2 (Peterson et al. 2004) and the uncertainty of $\log(\sigma_*)$ is 0.07 dex (Tremaine et al. 2002).

corresponds to a Markov chain length of one million, so for each quasar at least two million continuum spectra have been generated for comparison with the data.

The fitting results are tabulated in Table 4 and the best-fitting model spectra are shown in Fig. 3 as solid lines. For comparison, we also plot the corresponding model spectra without the Balmer edge absorption as dashed lines. The probability density of each parameter from the MCMC simulation is shown in Fig. 4. The optimal value ($X_{\rm O}$) of each parameter is taken as the best-fitting value of the parameters (i.e. the parameter set that provides the smallest χ^2 in the Markov chain). Because of the asymmetry of these probability distributions, the lower ($X_{\rm L}$) and upper ($X_{\rm U}$) boundaries at the 95 per cent confidence level of each parameter are determined in the following way:

$$\frac{\int_{X_{\rm L}}^{X_{\rm O}} p(X)\,{\rm d}X}{\int_{0}^{X_{\rm O}} p(X)\,{\rm d}X} = 0.95; \tag{8}$$

$$\frac{\int_{X_{\rm O}}^{X_{\rm U}} p(X)\,{\rm d}X}{\int_{X_{\rm O}}^{\infty} p(X)\,{\rm d}X} = 0.95. \tag{9}$$

Table 4. Physical parameters of 3C 95 and 4C 09.72 estimated by fitting their continuum spectra. Five parameters are estimated from the spectral fitting: BH spin a/M, accretion rate $L'/L_{\rm EDD} \equiv L/L_{\rm EDD} \times (3/4)[\mu + (2/3)]\mu$, polarization P, disc inclination i and Balmer edge optical depth τ_0. The spectral fitting is performed with MCMC simulations that generate chains to the convergence. The BH masses are estimated by kinetic measurements ($M_{\rm BH-KM}$ in Table 3). The first line of each object lists the best-fitting results, defined as the parameter set that provides the smallest χ^2. The second line of each object lists the most probable parameter values, defined as the peak value in the posterior probability distribution. The third line of each object lists the lower and upper 95 per cent boundary values of parameter estimates on both sides of the best-fitting values for $T = 8000$–$20\,000$ K, using equations (8) and (9), respectively. The fourth line lists the parameter boundary values estimated from a separate set of MCMC simulations, in which we have assumed that the Balmer edge absorption occurs in the disc annuli of $T = 8000$–$15\,000$ K. Similarly, the fifth line lists the parameter boundary values estimated with $T = 8000$–$25\,000$ K. We see that, except for τ_0, the spectral fitting does not depend on the specific choice of the Balmer edge temperature range.

	a/M	$L'/L_{\rm EDD}$	P (per cent)	i (°)	τ_0	χ^2/dof	$L/L_{\rm EDD}$
3C 95 (best-fitting)	0.030	0.070	1.48	70.4	0.32	4237.8/2637	0.28
Peak	0.65	0.067	1.37	51.6	0.45		0.11
$T = (8$–$20) \times 10^3$ K	0.0035–0.84	0.061–0.080	1.08–1.83	6.6–79.6	0.035–4.80		0.049–0.70
$T = (8$–$15) \times 10^3$ K	0.0054–0.82	0.062–0.084	1.10–1.86	8.1–82.7	0.055–9.51		0.050–1.11
$T = (8$–$25) \times 10^3$ K	0.0045–0.84	0.061–0.081	1.10–1.82	6.8–80.0	0.021–1.60		0.050–0.75
4C 09.72 (best-fitting)	0.0049	0.021	2.46	67.1	0.34	7678.7/3295	0.067
Peak	0.48	0.020	2.09	30.4	0.75		0.020
$T = (8$–$20) \times 10^3$ K	0.0024–0.76	0.018–0.027	1.49–3.25	3.5–78.3	0.035–4.04		0.014–0.20
$T = (8$–$15) \times 10^3$ K	0.0034–0.74	0.018–0.024	1.60–3.12	3.9–75.3	0.135–9.56		0.015–0.14
$T = (8$–$25) \times 10^3$ K	0.0034–0.77	0.018–0.027	1.47–3.09	3.3–74.8	0.036–1.96		0.015–0.15

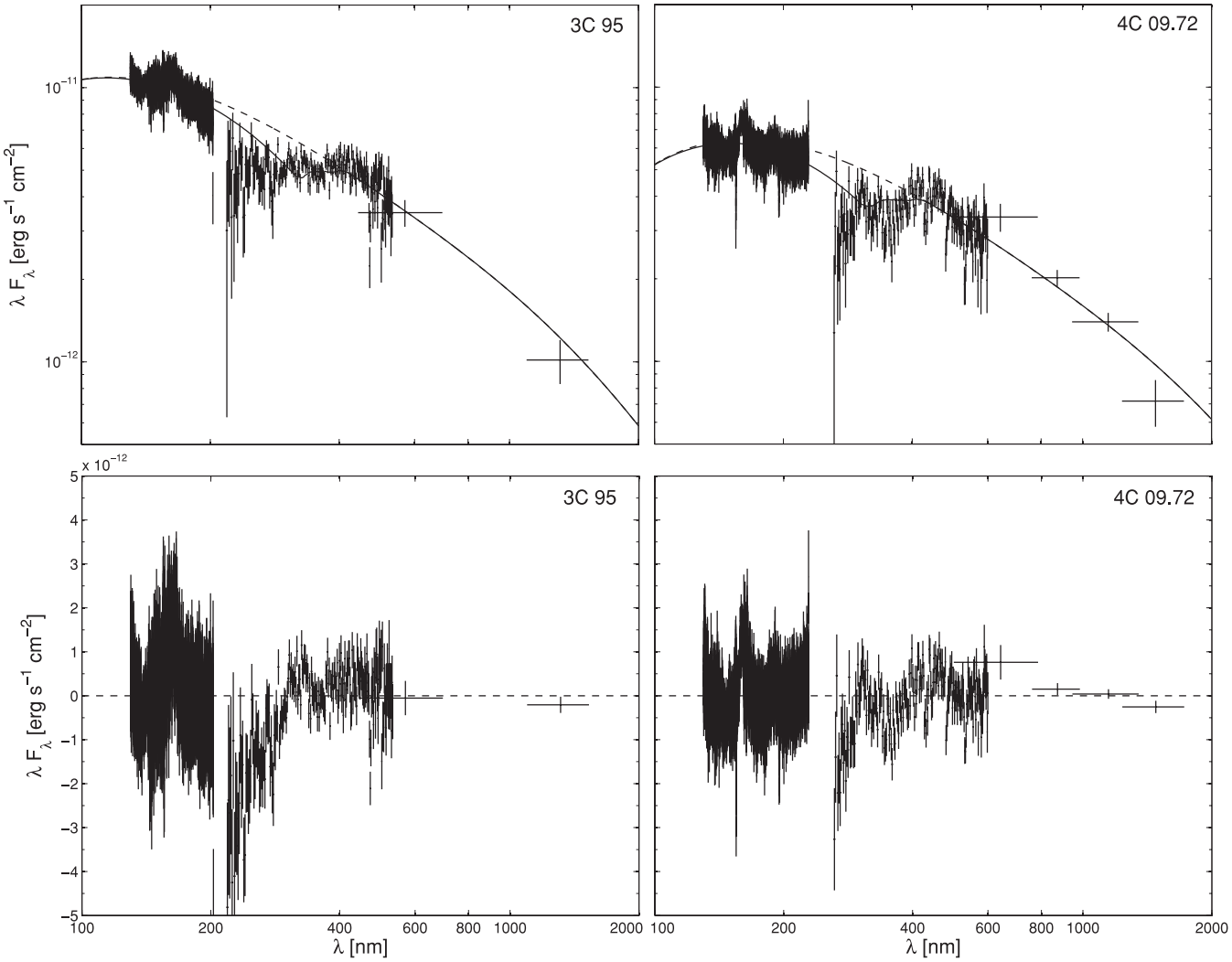

Figure 3. Best-fitting model spectra of 3C 95 and 4C 09.72. The upper panels show the observed spectra and the fitting results. The observed polarized spectra have been uniformly multiplied by a factor of $1/P$ for comparison with the UV total-light continuum. The solid lines are the best-fitting model spectra with the parameters tabulated in Table 4. The dashed lines are calculated with the same parameters, but without the Balmer edge absorption ($\tau_0 = 0$). The lower panels show the fitting residuals. Note that the vertical axis of the lower panels is in the linear scale. We see that the Balmer edge absorption is clearly revealed in the polarized continuum spectra of the quasars.

Here, $p(X)$ is the probability density of the parameter X. The correlations among the five fitting parameters of 3C 95 and 4C 09.72 are shown in Figs 5 and 6, respectively. In Table 4, we have provided both the best-fitting values and the most probable values for the parameters. The discrepancies between the best-fitting values and the most probable values can be large, for those parameters that are poorly constrained by the data (e.g. a/M, i). Nevertheless, for all parameters, the best-fitting values and the most probable values lie within their 1σ ranges.

5 RESULTS

5.1 Polarization of accretion disc emission

The continuum spectra of 3C 95 and 4C 09.72 from UV to NIR wavelengths can be sufficiently described by the standard accretion disc model with a prominent Balmer edge absorption, as shown in Fig. 3. The peak emissions of both 3C 95 and 4C 09.72 are at the wavelengths of 100–200 nm, which have been observed by the *HST*. The observed UV continuum spectra of the two quasars are indeed the optically thick thermal radiation from the inner part of the accretion disc. The polarized spectra from visible to NIR wavelengths are wavelength-independent scaled spectra of the disc's thermal emission. Therefore, the polarized spectra from visible to NIR wavelengths can be bridged with the total UV continua by adjusting the polarization fraction. The resulting continuum spectra from UV to NIR represent the thermal emission from a wide range of radii of the accretion discs of quasars.

The optical polarization of accretion disc emission can be determined by bridging the polarized visible-IR emission to the total emission at UV wavelengths. Both total emission and polarized emission, although at different wavelengths, follow the same multicolour thermal emission spectrum; hence, the polarization fraction can be well constrained by spectral fitting of the continuum thermal emission of accretion discs (see Fig. 4). The uncertainty of the optical polarization is Gaussian and is independent of other BH or accretion disc properties (see Figs 5 and 6). We emphasize that the polarization derived in this paper is the true polarization of the accretion

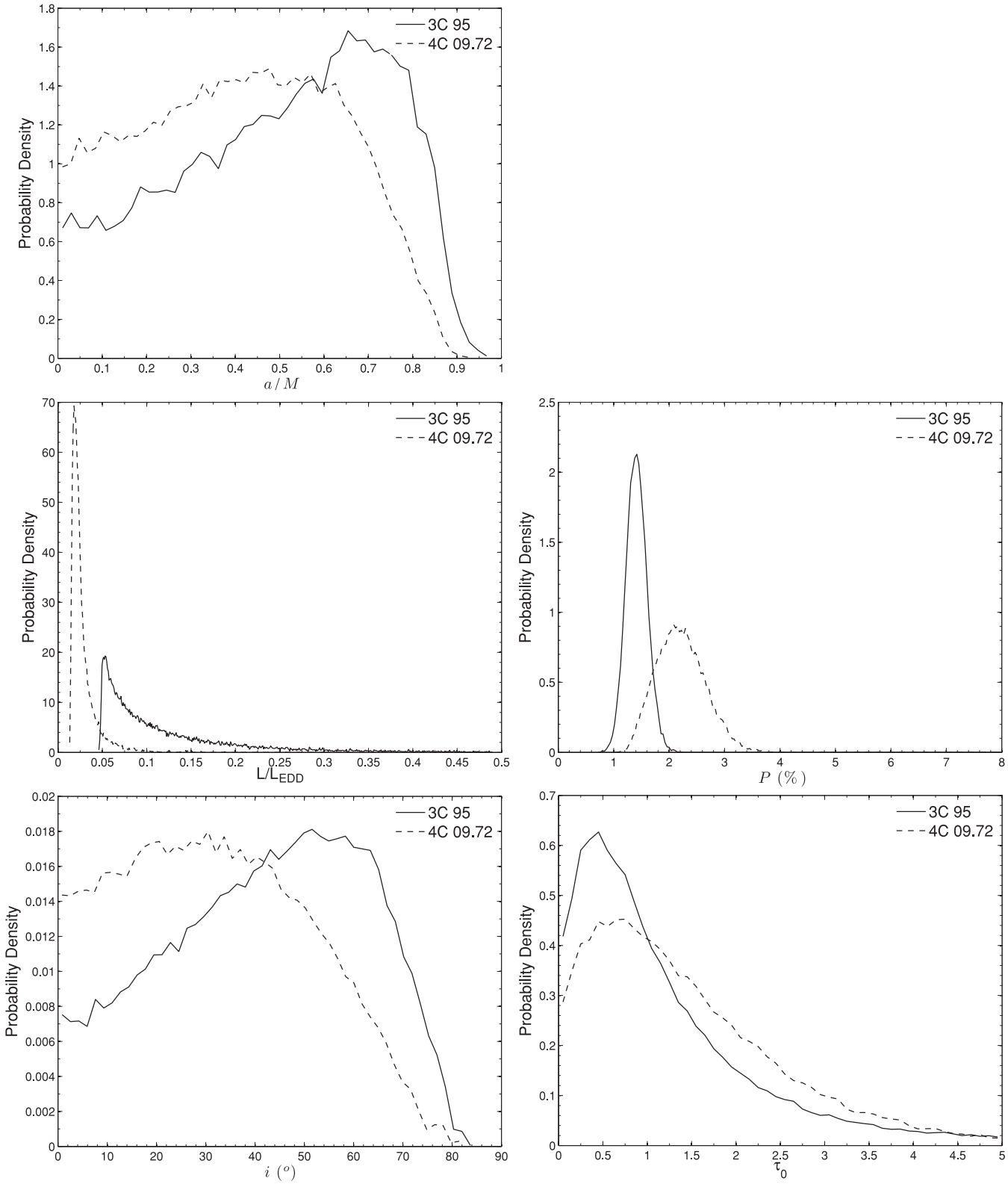

Figure 4. Posterior probability densities of the physical parameters of 3C 95 and 4C 09.72. For each object, the probability densities are computed from the MCMC of the last two million iterations in order to minimize the effect of the initial conditions. The accretion rate ($L/L_{\rm EDD}$) is computed from the effective accretion rate (L') and the inclination (i) of the fitting results. We see that the UV continuum and polarized optical continuum can well constrain the accretion rate and the polarization, and the Balmer edges revealed by the polarized optical continuum provide information on the inclination.

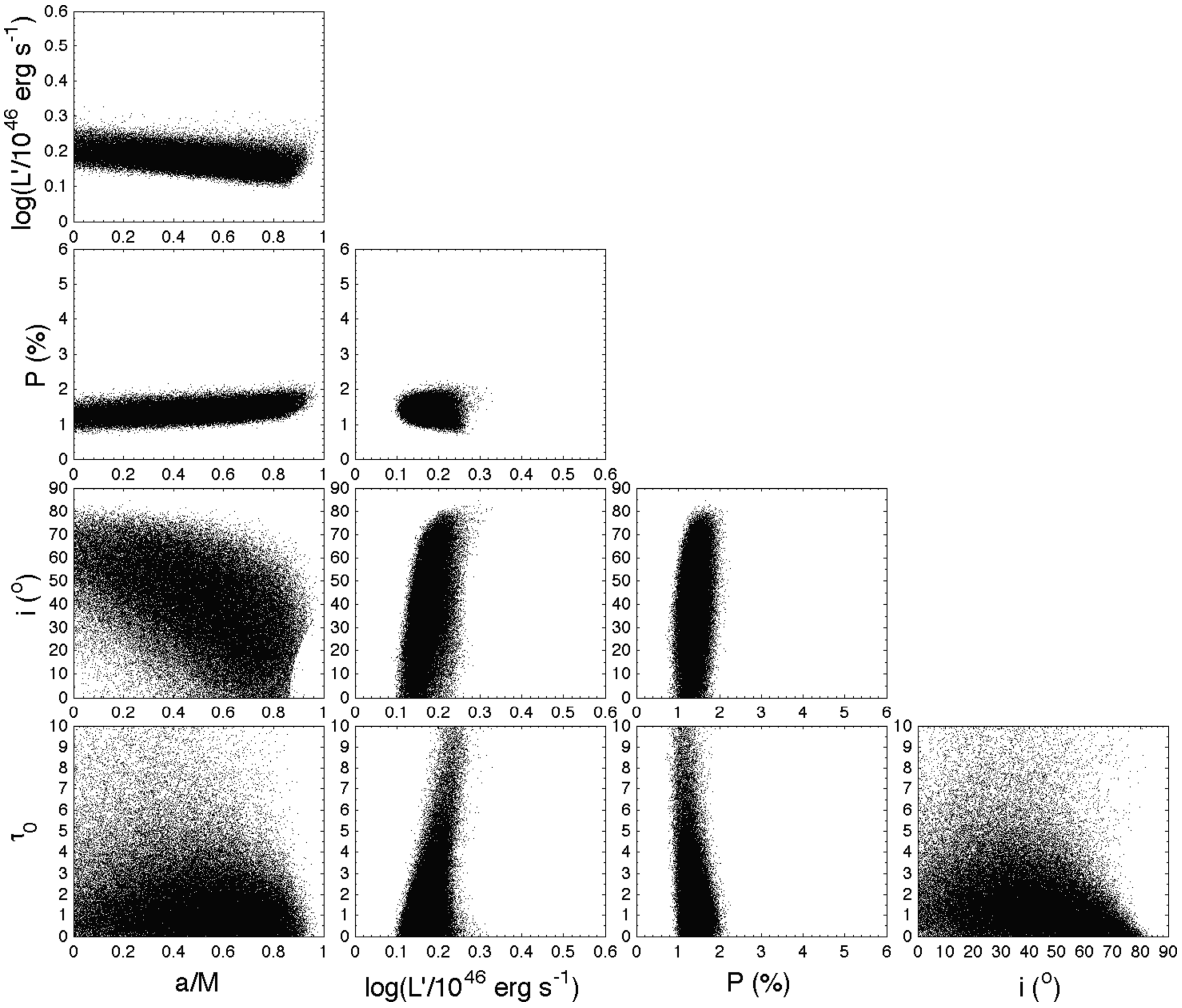

Figure 5. Correlation of the five fitting parameters of 3C 95. Each panel shows the joint posterior probability distribution between a pair of parameters, with each dot corresponding to a parameter set in the MCMC of the second half of the two million iterations.

disc emission, and we expect the true polarization to be larger than the observed polarization because of contamination from the host galaxy. The observed polarization fraction of both 3C 95 and 4C 09.72 is ∼1.0–1.5 per cent at wavelengths of 400–500 nm, and it gradually decreases to ∼0.5–1.0 per cent at 250 nm (Schmidt & Smith 2000; Kishimoto et al. 2008). These observations are consistent with our spectral fitting results, although we do not use the total light in visible wavelengths directly. In comparison with the true polarization obtained from spectral fitting, we find that, for 3C 95, there is little contamination from its host galaxy at 400–500 nm, but the contamination increases significantly for shorter wavelengths; for 4C 09.72, contamination from the host galaxy is significant for all visible and NIR wavelengths.

Spectral fitting to the accretion disc continuum from UV to NIR might constrain the BH and accretion disc properties. The disc's accretion rate is tightly constrained by the total luminosity of the accretion disc, a physical quantity that is derived from the polarized luminosity and the true polarization fraction (see Fig. 4). The accretion rate is only weakly correlated with the BH spin, as predicted by the standard thin disc model (see Figs 5 and 6). Also, the estimated accretion rates are significantly sub-Eddington, well within the range in which the standard thin disc model can be applied reliably. We have also performed continuum spectral fitting for 3C 95 and 4C 09.72 with the BH mass assumed as the fitting parameter (not shown in the paper). We obtained quantitatively very similar results, and the BH mass estimated from the spectral fitting is consistent with the kinetics estimates in Table 3. This suggests that their disc continuum spectra do not contain additional information on their BH masses (i.e. their BH mass uncertainties are dominated by the uncertainties in their kinematic mass estimates).

5.2 Revealed Balmer edge absorption

Prominent Balmer edge absorption features are found in the two continuum spectra, as shown in Fig. 3. The Balmer edge absorption is a result of the bound-free opacities in the accretion disc's atmosphere, which can only be seen in the disc's emission continuum with contamination from the host galaxy removed. Here, we confirm that the Balmer edge absorption for quasars is observable via polarized spectra in the visible wavelengths (i.e. Kishimoto et al. 2004, 2005, 2008). The predicted shape of the Balmer edge absorption combines the photoelectric absorption profile and the broadening as a result of the orbital motion. As shown in Fig. 3, the Balmer edge absorption fits the break of polarized spectra at ∼400 nm and connects to the UV continuum smoothly.

The observed Balmer edge absorption is broadened because of the orbital motion of the accretion disc. Because the Balmer edge opacity is proportional to the concentration of $n = 2$ hydrogen, the

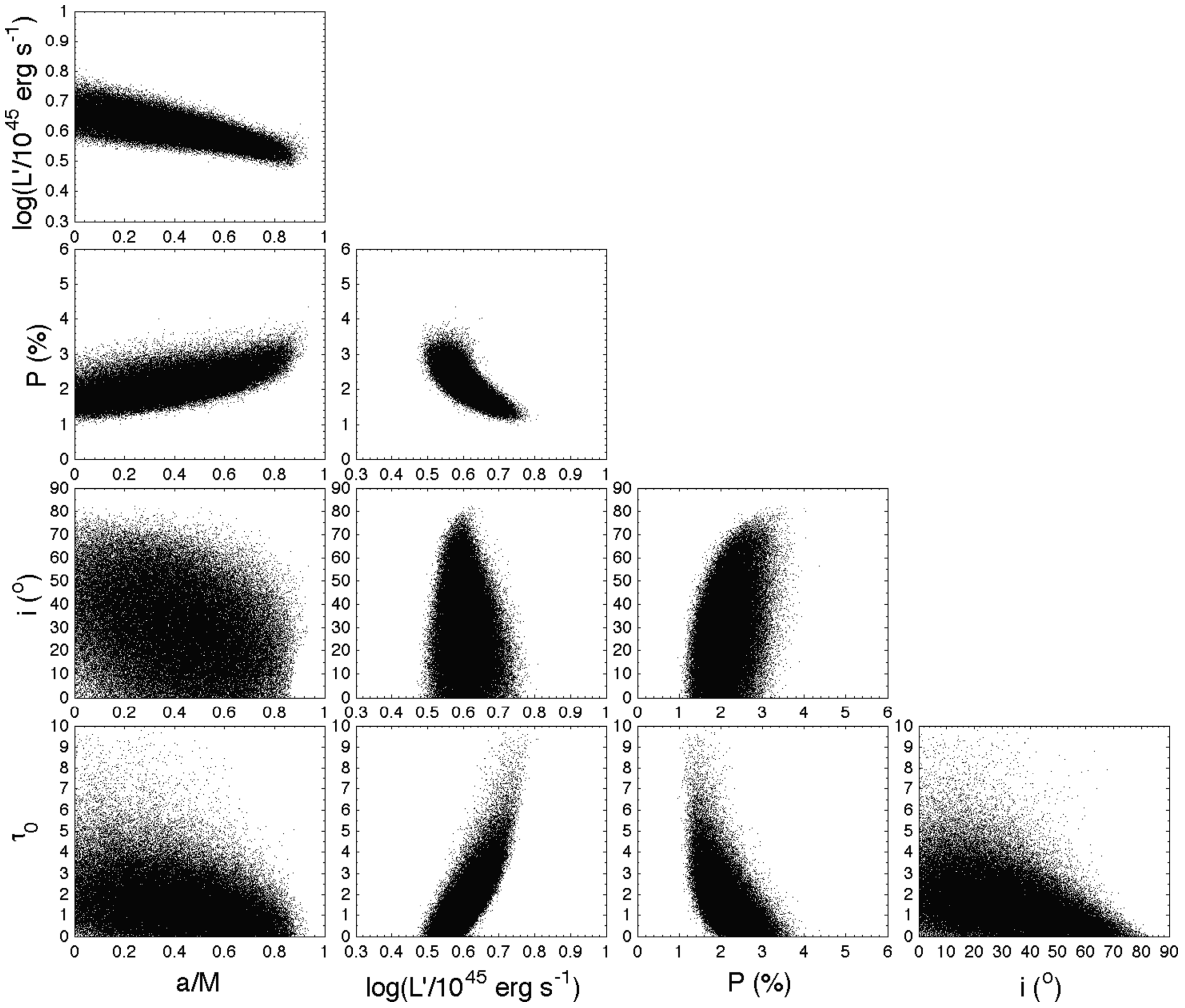

Figure 6. Correlation of the five fitting parameters of 4C 09.72. Each panel shows the joint posterior probability distribution between a pair of parameters, with each dot corresponding to a parameter set in the MCMC of the second half of the two million iterations.

Balmer edge absorption feature in the disc continuum is generated in a narrow annuli of the accretion disc in which the temperature is 8000–20 000 K. The inclination of the accretion disc significantly affects the broadening of the Balmer edge feature, because the broadening mostly depends on the line-of-sight projection of the orbital motion velocity of the specific Balmer-edge-generating annulus. From the spectral fitting, we find that (i) orbital motion is sufficient to account for the broadening of the revealed Balmer edges for 3C 95 and 4C 09.72 (Fig. 3) and (ii) the widths of the Balmer edges might constrain the disc inclination (Fig. 4). Noticeably, the edge-on geometry is confidently ruled out by fitting the emission spectra for 3C 95 and 4C 09.72 (Fig. 4), which is consistent with these being type 1 quasars. However, the spectral fitting cannot rule out the face-on geometry (Fig. 4), because of the intrinsic width of the Balmer edge from the $\nu/\nu_c^{-2.67}$ dependence of the photoelectric absorption cross-sections. We could assert that the most likely inclination of 3C 95 is larger than that of 4C 09.72; any further constraint of disc inclination by Balmer edge broadening is impeded by the relatively low signal-to-noise ratio of the Balmer edge feature, and the uncertainties of Balmer edge optical depths.

Spectral fitting to the accretion disc continuum from UV to NIR can determine the optical depth of the Balmer edge absorption. As shown in Table 4, the Balmer edge optical depths of 3C 95 and 4C 09.72 are large enough to create significant spectral features. The upper limit of the optical depth is constrained by the spectral fitting, as indicated by the posterior probability distribution shown in Fig. 4. We caution that, for a Balmer edge optical depth that is significantly larger than unity, the optically thin assumption might break down, and the full radiative transfer model of the accretion disc atmosphere is needed. After all, the best-fitting values and the most probable values of the optical depth for both quasars are found to be consistent with an optically thin absorption. With the bound-free cross-section of hydrogen at the Balmer edge ($\sigma_{\rm bf} = 1.3 \times 10^{-17}$ cm^2), we estimate the column density of excited ($n = 2$) hydrogen atoms to be 3×10^{15}–4×10^{17} cm^{-2} for 3C 95 and 3×10^{15}–3×10^{17} cm^{-2} for 4C 09.72. For the local thermal equilibrium, the implied neutral hydrogen column density on the accretion disc by the Balmer edge optical depth is estimated to be 10^{19}–10^{21} cm^{-2}. The neutral hydrogen column density is comparable to the neutral hydrogen column density of the Milky Way, which is consistent with the interpretation that the Balmer edge features originate on the accretion discs of quasars.

6 DISCUSSION AND CONCLUSION

The polarized continuum spectrum of a quasar at visible to NIR wavelengths, together with the total continuum spectrum at UV wavelengths, provides a unique opportunity to determine

the properties of accretion discs around SMBHs. In this paper, we have fitted the spectra of two type 1 quasars (3C 95 and 4C 09.72) to the standard thin accretion disc model with the Balmer edge absorption, using the BH masses determined from stellar dynamics and reverberation measurements. We have used the MCMC method to sample a parameter space of BH spin, accretion rate, polarization, disc inclination and Balmer edge optical depth.

We conclude that the polarized spectra of a quasar at visible and NIR wavelengths and total spectra in UV wavelengths can reveal the accretion disc emission, which is indeed the thermal emission of the optically thick and geometrically thin accretion disc. At UV wavelengths, the contamination from the host galaxy is negligible, so the total spectra reflect the emission spectra of the accretion disc. At visible and NIR wavelengths, the contamination buries the intrinsic accretion disc emission as well as the Balmer edge feature. However, the contamination does not exist in the polarized spectra. Therefore, the polarized spectra at visible and NIR wavelengths and the total spectra at UV wavelengths allow us to study the entire accretion disc. The true optical polarization of the accretion disc emission can be well constrained by bridging the total emission at UV and the polarized emission at visible. We find that 3C 95 and 4C 09.72 have significantly sub-Eddington accretion rates, and that their optical polarizations are 1.1–1.8 and 1.5–3.3 per cent (at the 95 per cent confidence level), respectively. The true optical polarization of the accretion disc derived from our continuum fitting is larger than the observed optical polarization, which indicates contamination from the host galaxy in the total optical continua of the quasars.

The absorption feature found at the Balmer edge is prominent and significantly broadened. We have found that the Balmer absorption feature for both investigated quasars can be reproduced by assuming an optically thin absorbing $n = 2$ hydrogen population corotating with the accretion disc at radii with effective temperatures between 8000 and 20 000 K. The Balmer edge feature is found to extend to UV wavelengths, whose width is the result of both photoelectric absorption cross-section and the line-of-sight projection of the orbital motion. The choice of the temperature range does not significantly affect the spectral fitting. For example, for the upper boundary of temperature varying from 15 000 to 25 000 K, we did not find any significant corresponding dependence of the BH parameters and the true optical polarization (see Table 4). However, we have found that the best-fitting Balmer edge optical depth (τ_0) is strongly dependent on the width of the Balmer absorption annulus. The wider the annulus is, the deeper the Balmer edge appears, and the τ_0 required to fit the data is smaller (see Table 4). Therefore, the estimation of neutral hydrogen on the surface of the accretion disc is also sensitive to the temperature range. The sensitivity study has suggested that a reasonable uncertainty in the exact location where the Balmer edge absorption occurs has a major effect on the depth of the Balmer edge feature, but it only has a minor effect on the broadening of the Balmer edge feature. Indeed, the broadening of the Balmer edge feature depends mostly on the disc inclination. The broadening of the Balmer edge features tentatively constrain the disc inclination of the two quasars.

Our fitting results show that the BH spin parameters of quasars cannot be constrained well from the spectral fitting up to $\sim$100 nm. As shown in Fig. 4 and Table 3, the posterior probability distribution of the BH spin is very wide. The best-fitting parameters for both 3C 95 and 4C 09.72 indicate non-rotating BHs; however, a full exploration of the parameter space indicates that a significant range of a/M between 0 to 1 is acceptable. This is because of the combination of the uncertainties in inclination, accretion rate and BH mass.

Figs 5 and 6 show a weak correlation between τ_0 and i. As expected, a larger τ_0 would produce a deeper absorption edge, which allows the widths of the Balmer edge feature to be better determined and the disc inclination to be better constrained. Indeed, the uncertainties in the observed Balmer edge depth play a major role in the uncertainty of inclination. For example, the two polarized spectra at wavelengths shorter than about 300 nm are obviously below the model predictions. The spectral features have been noticed by Kishimoto et al. (2004). They did not make an unambiguous identification and interpretation of these features, but they suggested that these might be related to Fe II absorption and possibly the Bowen resonance–fluorescence lines. Nevertheless, the relatively lower signal-to-noise ratios of the measurements of the polarized spectra at wavelengths shorter than about 300 nm do not seem to affect the results of fitting to the Balmer edge significantly. However, future better observations might allow identification and physical modelling of these features, which might make it possible to obtain a better determination of the Balmer edge.

The foreseeable improvement in tightening the inclination uncertainty is to have better polarized spectral observations around the Balmer edge in the future. In this paper, we have found that the Balmer edge optical depth and the disc inclination are particularly sensitive to the continuum emission at wavelengths of 300–400 nm. The current data have low signal-to-noise ratios in this wavelength range; using data with high signal-to-noise ratios in the future, it might be plausible to study the visible continuum of the quasar accretion discs and to constrain the Balmer edge absorption and the disc inclination. Furthermore, because the uncertainty in inclination angle will propagate into an uncertainty in the accretion rate for a given observed flux, a more accurate inclination will also result in a more accurate accretion rate. Therefore, a combination of a more accurate inclination and a well-observed peak emission will allow the BH mass and accretion rate to be determined accurately, leading eventually to an accurate measurement of BH spin.

ACKNOWLEDGMENTS

We thank Makoto Kishimoto for providing us with an electronic version of their published polarized spectra used in this paper. RYH thanks L. Zhu for a helpful discussion. We are very grateful to the first referee, Robert Antonucci, and to a second anonymous referee for their constructive criticisms and many helpful comments, which have allowed us to correct and improve the paper substantially. RYH acknowledges partial funding support by the Massachusetts Institute of Technology (MIT) Presidential Fellowship. SNZ also acknowledges partial funding support by the National Natural Science Foundation of China under grant nos. 11133002, 10821061, 10733010 and 10725313, and by the 973 Programme of China under grant 2009CB824800.

REFERENCES

Agol E., Blaes O., 1996, MNRAS, 282, 965
Alonso-Herrero A. et al., 2011, ApJ, 736, 82
Antonucci R., 1993, ARA&A, 31, 473
Bahcall J. N. et al., 1993, ApJS, 87, 1
Bentz M. C., Peterson B. M., Pogge R. W., Vestergaard M., Onken C. A., 2006, ApJ, 644, 133
Blandford R. D., Mckee C. F., 1982, ApJ, 255, 419

Cristiani S., Vio R., 1990, A&A, 227, 385
Czerny B., Hryniewicz K., Nikolajuk M., Sadowski A., 2012, MNRAS, 415, 2942
Davis S. W., Loar A., 2011, ApJ, 728, 98
Evans I. N., Koratkar A. P., 2004, ApJS, 150, 73
Ferrarese L., Merritt D., 2000, ApJ, 539, L9
Francis P. J., Hewett P. C., Foltz C. B., Chaffee F. H., Weymann R. J., Morris S. L., 1991, ApJ, 373, 465
Gelman A., Rubin D. B., 1992, Stat. Sci., 7, 457
Haario H., Laine M., Mira A., Saksman E., 2006, Stat. Comput., 16, 339
Hubeny I., Agol E., Blaes O., Krolik J. H., 2000, ApJ, 533, 710
Hubeny I., Blaes O., Krolik J. H., Agol E., 2001, ApJ, 559, 680
Kacprzak G. G., Churchill C. W., Evans J. L., Murphy M. T., Steidel C. C., 2011, MNRAS, 416, 3118
Kaspi S., Maoz D., Netzer H., Peterson B. M., Vestergaard M., Jannuzi B. T., 2005, ApJ, 629, 61
Kishimoto M., Antonucci R., Boisson C., Blaes O., 2004, MNRAS, 354, 1065
Kishimoto M., Antonucci R., Blaes O., 2005, MNRAS, 364, 640
Kishimoto M., Antonucci R., Blaes O., Lawrence A., Boisson C., Albrecht M., Leipski C., 2008, Nat, 454, 492
Krolik J. H., 1998, Active Galactic Nuclei: From the Central Black Hole to the Galactic Environment. Princeton Univ. Press, Princeton, NJ
Loar A., Netzer H., 1989, MNRAS, 238, 897
Loar A., Netzer H., Piran T., 1990, MNRAS, 242, 560
Lynden-Bell D., Pringle J. E., 1974, MNRAS, 168, 603
Marziani P., Sulentic J. W., Dultzin-Hcyan D., Calvani M., Moles M., 1996, ApJS, 104, 37
Nelson C. H., 2000, ApJ, 544, L91
Nelson C. H., Whittle M., 1996, ApJ, 465, 96
Neugebauer G., Green R. F., Matthews K., Schmidt M., Soifer B. T., Bennett J., 1987, ApJS, 63, 615
Novikov I., Thorne K. S., 1973, in de Witt C., de Witt B., eds, Black Holes. Gordon & Breach, New York, p. 422
Onken C. A., Ferrarese L., Merritt D., Peterson B. M., Pogge R. W., Vestergaard M., Wandel A., 2004, ApJ, 615, 645
Peterson B. M., 1993, PASP, 105, 247
Peterson B. M. et al., 2004, ApJ, 613, 682
Schmidt G. D., Smith P. S., 2000, ApJ, 545, 117
Shafee R., McClintock J. E., Narayan R., Davis S. W., Li L.-X., Remillard R. A., 2006, ApJ, 636, L113
Shakura N. I., Sunyaev R. A., 1973, A&A, 24, 337
Smith J. E., Robinson A., Young S., Axon D. J., Corbett E. A., 2005, MNRAS, 359, 846
Stockman H. S., Angel J. R. P., Miley G. K., 1979, ApJ, 227, L55
Telfer R. C., Zheng W., Kriss G. A., Davidsen A. F., 2002, ApJ, 565, 773
Tremaine S. et al., 2002, ApJ, 574, 740
Vestergaard M., Wilkes B. J., 2001, ApJS, 134, 1
Wills B. J., Brotherton M. S., 1995, ApJ, 448, L81
Zhang S. N., Cui W., Chen W., 1997, ApJ, 482, L155
Zheng W., Kriss G. A., Telfer R. C., Grimes J. P., Davidsen A. F., 1997, ApJ, 475, 469

APPENDIX A: ANALYTICAL EXPRESSIONS OF $x_{\rm in}$, η AND $R_{\rm R}$

We provide analytical expressions of the (dimensionless) innermost circular orbit $x_{\rm in}$, the radiative efficiency η and the GR correction term $R_{\rm R}$, as functions of the BH spin a/M (Krolik 1998). The innermost circular orbit $x_{\rm in}$ is

$$x_{\rm in} = 3 + z_2 - \sqrt{(3 - z_1)(3 + z_1 + 2z_2)}, \tag{A1}$$

for which z_1 and z_2 can be computed from the BH spin (a/M) as

$$z_1 = 1 + [1 - (a/M)^2]^{1/3}[(1 + a/M)^{1/3} + (1 - a/M)^{1/3}], \tag{A2}$$

and

$$z_2 = \sqrt{3(a/M)^2 + z_1^2}. \tag{A3}$$

The radiative efficiency is related to the innermost circular orbit as

$$\eta = 1 - \frac{x_{\rm in}^2 - 2x_{\rm in} + (a/M)x_{\rm in}^{1/2}}{x_{\rm in}\sqrt{x_{\rm in}^2 - 3x_{\rm in} + 2(a/M)x_{\rm in}^{1/2}}}. \tag{A4}$$

The GR correction term $R_{\rm R}$ is a function of radius x as

$$R_{\rm R}(x) = \frac{C(x)}{A(x)}, \tag{A5}$$

where $A(x)$ is

$$A(x) = 1 - \frac{2}{x} + \frac{(a/M)^2}{x^2}, \tag{A6}$$

and $C(x)$ is

$$\begin{aligned} C(x) = 1 &- \frac{y_{\rm in}}{y} - \frac{3(a/M)}{2y}\log\left(\frac{y}{y_{\rm in}}\right) \\ &- \frac{3(y_1 - a/M)^2}{yy_1(y_1 - y_2)(y_1 - y_3)}\log\left(\frac{y - y_1}{y_{\rm in} - y_1}\right) \\ &- \frac{3(y_2 - a/M)^2}{yy_2(y_2 - y_1)(y_2 - y_3)}\log\left(\frac{y - y_2}{y_{\rm in} - y_2}\right) \\ &- \frac{3(y_3 - a/M)^2}{yy_3(y_3 - y_2)(y_3 - y_1)}\log\left(\frac{y - y_3}{y_{\rm in} - y_3}\right). \end{aligned} \tag{A7}$$

Here, $y = \sqrt{x}$, $y_{\rm in} = \sqrt{x_{\rm in}}$ and y_1, y_2 and y_3 are three roots of the following equation:

$$x^3 - 3x + 2a/M = 0. \tag{A8}$$

This paper has been typeset from a TEX/LATEX file prepared by the author.